The Astrophysical Journal, 933:102 (8pp), 2022 July 1 https://doi.org/10.3847/1538-4357/ac7564
© 2022. The Author(s). Published by the American Astronomical Society.
OPEN ACCESS

iPTF14hls in the Circumstellar Medium Interaction Model: A Promising Candidate for a Pulsational Pair-instability Supernova

Ling-Jun Wang[1], Liang-Duan Liu[2,3], Wei-Li Lin[4], Xiao-Feng Wang[4,5], Zi-Gao Dai[6], Bing Li[1], and Li-Ming Song[1]
[1] Astroparticle Physics, Institute of High Energy Physics, Chinese Academy of Sciences, Beijing 100049, People's Republic of China; wanglingjun@ihep.ac.cn, liuld@ccnu.edu.cn
[2] Institute of Astrophysics, Central China Normal University, Wuhan 430079, People's Republic of China
[3] Key Laboratory of Quark and Lepton Physics (Central China Normal University), Ministry of Education, Wuhan 430079, People's Republic of China
linwl@mail.tsinghua.edu.cn
[4] Physics Department and Tsinghua Center for Astrophysics, Tsinghua University, Beijing 100084, People's Republic of China
[5] Beijing Planetarium, Beijing Academy of Sciences and Technology, Beijing 100044, People's Republic of China
[6] CAS Key Laboratory for Research in Galaxies and Cosmology, Department of Astronomy, University of Science and Technology of China, Hefei 230026, People's Republic of China
Received 2022 January 11; revised 2022 May 30; accepted 2022 May 31; published 2022 July 7

Abstract

iPTF14hls is a luminous Type II supernova (SN) with a bumpy light curve whose origin remains under debate. It maintains a roughly constant effective temperature and luminosity for about 600 days after discovery, followed by a slow decay. About ∼1000 days after discovery, the light curve transitions to a very steep decline. A spectrum taken during this steep-decline phase shows clear signatures of a shock interaction with a dense circumstellar medium (CSM). Here, we explore the possibility of iPTF14hls as an interaction-powered SN. The light curve of iPTF14hls can be fitted with wind-like CSMs. Analytic modeling indicates that iPTF14hls may have undertaken six episodes of mass loss during the last ∼200 yr. Assuming that the 1954 eruption triggered the last mass-loss episode, the stellar wind velocity is determined to be $40-70\,\mathrm{km\,s^{-1}}$, depending on different models. Mass-loss rates are in the range 0.4–$3.3 M_{\odot}\,\mathrm{yr^{-1}}$. The inferred total mass of the ejecta and CSMs ($M_{\rm ej}+M_{\rm CSMs}\simeq 245 M_{\odot}$) supports the idea that iPTF14hls may be a candidate for a (pulsational) pair-instability SN. Discoveries and observations of similar stellar explosions will help us to understand these peculiar SNe.

Unified Astronomy Thesaurus concepts: Type II supernovae (1731)

1. Introduction

iPTF14hls is a nearby ($z=0.0344$) peculiar supernova (SN) first discovered in R band on 2014 September 22 UT by the Intermediate Palomar Transient Factory (iPTF) wide-field camera survey (Arcavi et al. 2017). It was classified as a Type II-P (Filippenko 1997) SN according to its spectroscopic features (Li et al. 2015). The light curves of iPTF14hls last for more than 1200 days (Sollerman et al. 2019) and are bumpy in the first 500 days after discovery. The velocities of the hydrogen lines of iPTF14hls decline from 8000 to 6000 $\mathrm{km\,s^{-1}}$ over 600 days, during which the iron lines (Fe II λ5169) stay at a constant velocity of 4000 $\mathrm{km\,s^{-1}}$. The effective temperature of iPTF14hls is roughly constant ($T\approx 6000$ K). The spectral evolution of iPTF14hls is also very slow compared to typical SNe II-P (Arcavi et al. 2017).

600 days after discovery, the evolution of iPTF14hls speeds up. In particular, the light curve transitions to a very steep decline ∼1000 days after discovery (Sollerman et al. 2019). During this time, a spectrum taken on day 1153 after discovery reveals a clear signature of a shock interaction with a dense circumstellar medium (CSM; Andrews & Smith 2018). Interestingly, Yuan et al. (2018) report the detection of a variable γ-ray source in the energy band from 0.2 to 500 GeV, which is positionally and temporally consistent with iPTF14hls. However, it cannot be confirmed whether this γ-ray source is associated with iPTF14hls or a blazar candidate.

Original content from this work may be used under the terms of the Creative Commons Attribution 4.0 licence. Any further distribution of this work must maintain attribution to the author(s) and the title of the work, journal citation and DOI.

Several models have been proposed or discussed to interpret iPTF14hls (Andrews & Smith 2018; Chugai 2018; Dessart 2018; Soker & Gilkis 2018; Wang et al. 2018; Woosley 2018; Gofman & Soker 2019; Liu et al. 2019; Modjaz et al. 2019; Kaplan & Soker 2020; Moriya et al. 2020; Uno & Maeda 2020). Until now, however, no single model has been able to interpret all the observational features of iPTF14hls. The late-time spectrum of iPTF14hls exhibits a double-peak intermediate-width Hα line indicating strong ejecta–CSM interaction (CSI). Together with the early bumps and the late steep decline of the light curves of iPTF14hls, Andrews & Smith (2018) proposed that variations in the density structure of the CSM could explain the multiple peaks of the light curve. But they did not model the long-lived light curve of iPTF14hls based on successive collisions of circumstellar shells and SN ejecta in detail. In previous studies, the CSI model has been applied to a variety of SNe with bumpy light curves (Wang et al. 2016; Liu et al. 2018; Li et al. 2020). Observations reveal that bumpy features are very common (Hosseinzadeh et al. 2021) in the light curves of superluminous SNe (SLSNe; Quimby et al. 2011; Gal-Yam 2012; Moriya et al. 2018; Gal-Yam 2019; Inserra 2019). This indicates that mass loss of massive stars during their final stages of evolution is common (Smith 2014) if the bumps in the light curves of SLSNe are caused by CSIs. Signatures for the presence of nearby CSMs have also been reported for several SNe II-P/II-L/IIb (Quimby et al. 2007; Gal-Yam et al. 2014; Khazov et al. 2016; Yaron et al. 2017; Hosseinzadeh et al. 2018; Rui et al. 2019; Bruch et al. 2021; Jacobson-Galá et al. 2022) by the detection of flash-ionized emission lines from dense circumstellar wind.

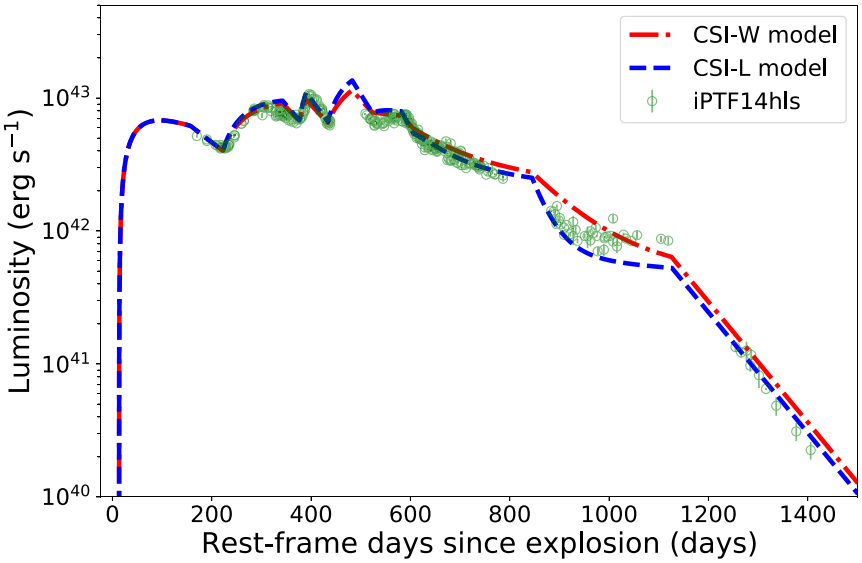


Figure 1. Fits of the CSI-L model and the CSI-W model to the bolometric luminosity of iPTF14hls. The data are taken from Arcavi et al. (2017) and Sollerman et al. (2019).

The CSI model is also able to produce some rapidly varying light curves that can be applied to the emerging fast blue optical transients (Tolstov et al. 2019; Wang et al. 2019b; Leung et al. 2020, 2021; Xiang et al. 2021; Gal-Yam et al. 2022; Pellegrino et al. 2022). This is also an appealing factor of the CSI model, because the third peak (see Figure 1 below) in the light curve of iPTF14hls varies so rapidly that it can only be fitted by a CSI or other instantaneously released energy (Wang et al. 2018; Kaplan & Soker 2020).

Based on the above considerations, here we explore the possibility of interpreting iPTF14hls as a multiple-interaction-powered SN. We apply the semianalytic multiple CSI model (Liu et al. 2018) to iPTF14hls to infer its explosion energy, ejecta mass, and CSM parameters, which allow us to consider the mass-loss history of the progenitor system. The semianalytic model is based on a spherically symmetric explosion with optically thick CSMs in spheric geometry (Chatzopoulos et al. 2012). As a result, the model predicts a stationary photosphere, inconsistent with the observed photospheric velocities. However, such a model can be improved by considering a clumpy CSM (Chugai & Danziger 1994) or an asymmetric disk-like medium embedded within the spherically expanding ejecta (Smith 2017; Andrews & Smith 2018; Suzuki et al. 2019). The semianalytic model is computationally efficient and can give a convenient estimate of the relevant parameters.

This paper is structured as follows. The models and fitting results are presented in Section 2. The mass-loss history is derived in Section 3. A discussion and conclusions are given in Section 4.

2. Models and Results

2.1. CSI Model

The CSI model assumes that the ejecta expand at a constant velocity $v_{\rm SN}$, with an inner power-law density profile ($\rho \propto r^{-\delta}$ with $\delta < 3$), surrounded by a steep outer power-law profile ($\rho \propto r^{-n}$ with $n > 5$; Parker 1961; Chevalier 1982; Chevalier & Fransson 1994). The Lagrangian coordinate for the transition from the inner flat profile to the outer steep profile is denoted as x_0 (Chatzopoulos et al. 2012). In this paper, we set $\delta = 0$, $x_0 = 0.7$.

The density profiles of the CSMs are also assumed in a power-law form $\rho \propto r^{-s}$. The CSMs are ejected by SN progenitors during their evolution to the final collapse. Usually, two kinds of density profiles of CSMs are considered, namely the stellar wind with $s = 2$ or a uniform shell with $s = 0$. In a multiple CSI model (Liu et al. 2018), we denote the mass of the ith CSM as $M_{{\rm CSM},i}$. The inner radius of the ith CSM is denoted as $R_{{\rm in},i}$. Similarly, the CSM density at $R_{{\rm in},i}$ is denoted as $\rho_{{\rm in},i}$.

The collision of the ejecta with the CSM results in the formation of a forward shock (FS) propagating into the CSM and a reverse shock (RS) propagating into the ejecta. The dynamical evolutions of the FS and RS are described by self-similar solutions (Chevalier 1982). Both the FS and RS convert the kinetic energy of the homologously expanding ejecta into radiation that powers the SN light curve. Based on these self-similar solutions, one can derive the expression for the FS and RS input luminosity that is produced from the CSI. The input luminosities of the FS and RS have the same temporal index (Chatzopoulos et al. 2012; Moriya et al. 2013b; Wang et al. 2019a):

$$L_{\rm inp,FS}(t) = L_{\rm FS,tr}\left(\frac{t}{t_{\rm tr}}\right)^{\alpha}, \quad L_{\rm inp,RS}(t) = L_{\rm RS,tr}\left(\frac{t}{t_{\rm tr}}\right)^{\alpha}, \qquad (1)$$

where the temporal index is

$$\alpha = \frac{2n + 6s - ns - 15}{n - s}, \qquad (2)$$

$t_{\rm tr}$ is the characteristic time of dynamical evolution, and $L_{\rm inp,FS}$ and $L_{\rm inp,RS}$ are the characteristic input luminosities of the FS and RS, respectively. These characteristic physical quantities depend on the nature of the CSM and the SN explosion, and the specific expressions are given in Liu et al. (2020). The heating from the FS terminates when all the available optically thick CSM has been swept up, by which one can obtain the FS termination timescale $t_{{\rm FS},*}$. Similarly, the RS termination time $t_{{\rm RS},*}$ is determined when all the ejecta $M_{\rm ej}$ have been swept up.

The input luminosities of the FS and RS from ith CSI are:

$$L_{\rm inp,CSM,}i,{\rm FS}(t) = \epsilon_{{\rm FS},i} L_{{\rm inp,FS},i}(t), \quad (3)$$

$$L_{\rm inp,CSM,}i,{\rm RS}(t) = \epsilon_{{\rm RS},i} L_{{\rm inp,RS},i}(t), \quad (4)$$

respectively. Here, $\epsilon_{\rm FS}$ and $\epsilon_{\rm FS}$ are the respective conversion efficiencies from kinetic energy to radiation by the FS and RS. Chatzopoulos et al. (2012) assume that all the kinetic energy of the SN ejecta converts efficiently to radiation, that is, $\epsilon_{\rm FS} = \epsilon_{\rm RS} = 1$. It may be reasonable for the case $M_{\rm CSM} \gg M_{\rm ej}$, but, on the contrary, this assumption is unrealistic for $M_{\rm CSM} \ll M_{\rm ej}$ (van Marle et al. 2010; Moriya et al. 2013a). Because of our poor knowledge of the physical process of converting the kinetic energy to radiation, we set $\epsilon_{\rm FS}$ and $\epsilon_{\rm RS}$ as independent parameters. After traversing a CSM, the ejecta will grow in mass and collide with the next CSM. Thus, the ejecta mass of the ith interaction is

$$M_{{\rm ej},i} = M_{{\rm ej},i-1} + M_{{\rm CSM},i-1}. \quad (5)$$

Previous studies of multiple-interaction models (Liu et al. 2018; Li et al. 2020) have usually assumed that an RS develops at every shell collision. However, whether an RS develops depends on the density structure and the preshock pressure. For the first collision of a "cold" SN ejecta and a "cold" CSM, both an FS and an RS would develop. Due to the preheated high pressure of the first FS, in successive collisions of CSM shells, RSs do not always develop, or they are at least very weak, with less effective contributions to the total luminosity. Therefore, in our calculation, we only consider the contributions from FSs and the first RS, and neglect the contributions from the rest of the RSs.

Considering that the expansion velocity of the CSM is much lower than the typical velocity of the SN ejecta, a fixed photosphere inside the CSM is usually adopted (Chatzopoulos et al. 2012; Liu et al. 2018). Under this assumption, the theoretical bolometric light curves contributed by the FS and RS of the ith collision are given by

$$L_{i,{\rm FS}}(t) = \frac{1}{t_{{\rm diff},i,{\rm FS}}} \exp\left(-\frac{t}{t_{{\rm diff},i,{\rm FS}}}\right) \times \int_0^t \exp\left(\frac{t'}{t_{{\rm diff},i,{\rm FS}}}\right) L_{{\rm inp,CSM,}i,{\rm FS}}(t')dt', \quad (6)$$

$$L_{i,{\rm RS}}(t) = \frac{1}{t_{{\rm diff},i,{\rm RS}}} \exp\left(-\frac{t}{t_{{\rm diff},i,{\rm RS}}}\right) \times \int_0^t \exp\left(\frac{t'}{t_{{\rm diff},i,{\rm RS}}}\right) L_{{\rm inp,CSM,}i,{\rm RS}}(t')dt', \quad (7)$$

respectively. Here, $t_{{\rm diff},i,{\rm FS}}$ and $t_{{\rm diff},i,{\rm RS}}$ are the respective diffusion times of the FS and RS of the ith CSM. The theoretical bolometric light curve of N times interactions is given by

$$L(t) = \sum_{i=1}^{N} [L_{i,{\rm FS}}(t) + L_{i,{\rm RS}}(t)]. \quad (8)$$

After $t_{i,{\rm FS},*}$ and $t_{i,{\rm RS},*}$, the luminosity input from the FS and RS ceases in the CSI models, and the decline in luminosity is predicted to be exponential.

To handle the diffusion of the shock energy, different authors use different recipes. Liu et al. (2018) adopted a diffusion timescale in the optically thick CSM for both the FS and RS:

$$t_{{\rm diff},i,{\rm FS}} = t_{{\rm diff},i,{\rm RS}} = \sum_{j=i}^{N} \frac{\kappa_j M_{{\rm CSM,th},j}}{\beta c R_{\rm ph}}, \quad (9)$$

where N is the total number of CSMs, $\beta \simeq 13.8$ is a constant (Arnett 1982), c is the speed of light, $R_{\rm ph}$ is the photospheric radius of the outermost CSM, κ_j, and $M_{{\rm CSM,th},j} \simeq M_{{\rm CSM},j}$ are the optical opacity and optically thick mass of the jth CSM, respectively. We denote the recipe used in Liu et al. (2018) as CSI-L.

Wheeler et al. (2017) assume that the shocks are located in the center of the ejecta, that is, in the original spirit of Arnett (1982). In this situation, the diffusion time of the ith CSI is

$$t_{\rm diff,i,FS} = t_{\rm diff,i,RS} = \frac{\kappa M_{\rm ej}}{\beta c R_{\rm ph}} + \sum_{i=1}^{N} \frac{\kappa_i M_{{\rm CSM,th},i}}{\beta c R_{\rm ph}}, \quad (10)$$

where κ is the optical opacity of the ejecta. To be distinctive, we hereafter denote the recipe in Wheeler et al. (2017) as CSI-W.

However, the FS and RS are not centrally concentrated, and move within the CSM and ejecta, respectively. The assumption of a deeply located power source is approximately appropriate for the RS, but is not true for the FS. As one may expect, different recipes have different advantages and shortcomings. The CSI-W model can better handle the RS luminosity, while the CSI-L model handles the FS luminosity better. The models can be improved by combining the advantages of the CSI-L and CSI-W models. We can set the diffusion time of the FS as is done in the CSI-L model, while setting the diffusion time of the RS as is done in the CSI-W model, that is:

$$t_{\rm diff,i,FS} = \sum_{j=i}^{N} \frac{\kappa_j M_{{\rm CSM,th},j}}{\beta c R_{\rm ph}}, \quad (11)$$

$$t_{\rm diff,i,RS} = \frac{\kappa M_{\rm ej}}{\beta c R_{\rm ph}} + \sum_{i=1}^{N} \frac{\kappa_i M_{{\rm CSM,th},i}}{\beta c R_{\rm ph}}. \quad (12)$$

Such a treatment is denoted as the CSI-LW model, and the Python code is available on GitHub,[7] with version 1.0 archived in Zenodo (Wang & Yu 2022).

A comparison of the fitting results of the CSI-L model and the CSI-W model is given in Figure 1, and the fitting parameters are listed in the Table 1. With the same fitting parameters, the theoretical light curve of the CSI-LW model is shown in Figure 2. The model parameters were varied manually, until reasonable agreement between the observational data and the theoretical model was found. The initial slow decline of the light curve favors a small $n < 9$ and wind-like CSMs. So we set $n = 7$ and $s = 2$. With these values, $\alpha = -0.6$. The spike (the third peak) in the light curve at ~400 days after explosion can only be fitted by a CSM much lighter than the ejecta. The opacity of the ejecta and CSMs is $\kappa = 0.34\ {\rm cm^2\ g^{-1}}$ (Matzner & McKee 1999), which is the Thomson electron-scattering opacity for fully ionized solar metallicity material. We find that in order to get a close fit to the light curve of iPTF14hls, six wind-like CSM shells are

[7] CatFit codebase: https://github.com/Lingjun-Wang/CatFit.

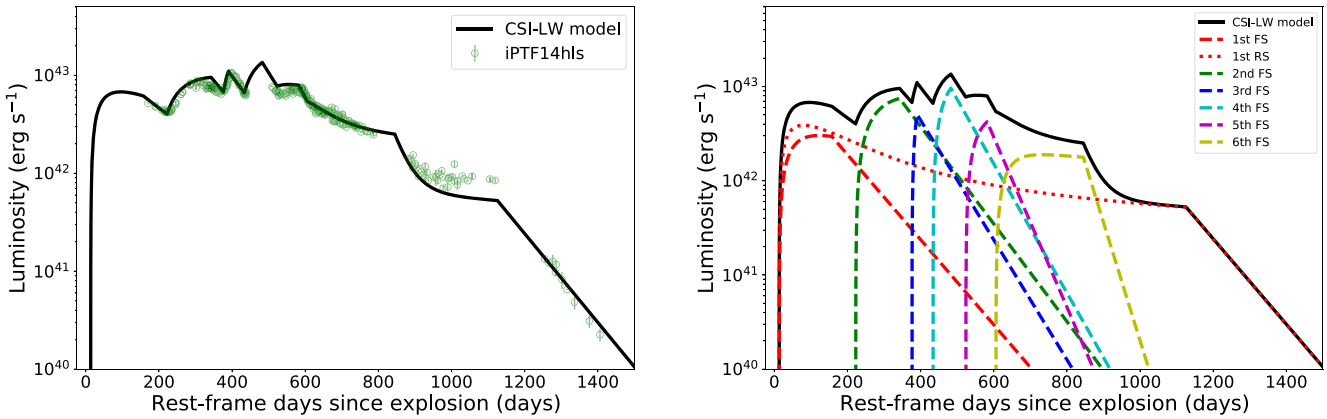


Figure 2. The fit to the bolometric luminosity (left panel) of iPTF14hls by the CSI-LW model. The contributions from the FSs and RS of the ith CSM are plotted in the right panel. The FS emissions are plotted with the dashed lines, while the first RS is plotted with the red dotted line.

Table 1
Model Parameters for iPTF14hls Based on the Pure CSI Model

Ejecta Properties						
$M_{\rm ej}(M_\odot)$	75					
$v_{\rm sn}$ (km s^{-1})	5200					
δ	0					
n	7					
CSM Properties						
	1st	2nd	3rd	4th	5th	6th
$M_{\rm CSM}(M_\odot)$	20	25.5	8	25	22	70
$R_{\rm in}(10^{15}$ cm)	0.6	10	16	18	21	23.5
$\rho_{\rm in}(10^{-15}$ g cm$^{-3})$	1200	7.2	6.0	5.0	3.2	2.2
$\epsilon_{\rm FS}$	0.02	0.09	0.26	0.2	0.09	0.04
$\epsilon_{\rm RS}$	0.4	0	0	0	0	0

required. The CSI model predicts an exponential decay of the light curve after the FS sweeps up all the CSMs or the RS sweeps up all the ejecta. The exponential decay of the light curve starting from ∼1100 days after explosion is contributed by the first RS (see Figure 1).

Given the same fitting parameters, Figure 1 shows that the theoretical light curve of CSI-L is brighter than that of CSI-W during the early phase of the light curve, but becomes dimmer during the late stage. This can be easily understood because the diffusion time in CSI-L is shorter and the emission diffuses out earlier.

One of the most influential parameters on the theoretical light curve is the inner radius of the ith CSM $R_{{\rm in},i}$, which determines the onset times of the interactions. In CSI-W, the ejecta mass $M_{\rm ej}$ affects the maximum and the width of the light curve, with a higher ejecta mass leading to a long-lived RS emission. The larger the CSM mass, the longer the light curve. For the pure CSI model, where only CSIs are the source for powering the SN light curve, the first RS has a long duration and contributes mainly to the first peak and the late-time steep decline. The explosion energy of iPTF14hls is estimated to be (Chevalier & Fransson 1994; Chatzopoulos et al. 2012)

$$E_{\rm SN} = \frac{(3-\delta)(n-3)}{2(5-\delta)(n-5)} M_{\rm ej}(x_0 v_{\rm SN})^2 = 1.2\times10^{52}\ {\rm erg}, \quad (13)$$

of which 5.5×10^{50} erg was emitted as visual light.

2.2. CSI Plus ^{56}Ni Model

From Table 1, we see that in the pure CSI model the progenitor has a zero-age main-sequence mass $M_{\rm zams}\simeq M_{\rm ej}+\Sigma M_{\rm CSMs}\simeq 245.5M_\odot$. The true value of $M_{\rm zams}$ may be higher than the value given here, to account for other pre-explosion mass-loss processes and the massive compact remnant, if the progenitor of iPTF14hls was not completely disrupted. For such massive stars, it is expected that some amount of ^{56}Ni is synthesized during the SN explosion (Heger & Woosley 2002; Umeda & Nomoto 2002).

In addition, in the pure CSI model the initial slow decline of the light curve can only be fitted with a CSI in which the RS emission dominates over the FS emission. This results in an $\epsilon_{\rm FS}=0.02$, which is exceptionally small compared to the $\epsilon_{\rm FS}$ of other CSMs. The initial decline can also be fitted with a CSM whose mass $M_{\rm CSM}\gtrsim 20M_\odot$, so that the FS emission lasts for more time, having a similar time dependence as the RS. This is because the heating rates of the FS and RS have the same power-law index (see Equation (1)). However, with such a massive CSM, it will be difficult to fit the exponential decline starting ∼1100 days after explosion (see Figure 2), because the large total mass ($M_{\rm ej}+\Sigma M_{\rm CSMs}$) results in a shallow exponential decline.

Based on the above considerations, we explore the possibility of fitting the initial decline of the light curve by ^{56}Ni decay. The fitting result is presented in Figure 3, with the fitting parameters listed in Table 2. The gray opacity to the ^{56}Ni cascade decay photons is $\kappa_\gamma=0.027\ {\rm cm^2\ g^{-1}}$ (Colgate et al. 1980; Swartz et al. 1995). In this model, the explosion energy is very close to the value given in Equation (13).

It is found that the observed light curve around ∼1000 days after explosion declines according to $L\propto t^{-0.3}$ (see Figure 3), while the theoretical light curve with $n=7$ and $s=2$ gives $L\propto t^{-0.6}$. This is the reason why there is some deviation between the theoretical light curve and the observational data. Actually, $L\propto t^{-0.3}$ is consistent with $n=12$ and $s=2$. Such an outer density profile for the ejecta is expected for the envelopes of red supergiant (RSG) progenitors, while $n=7$ can be found in the envelopes of more compact progenitors (Matzner & McKee 1999; Chatzopoulos et al. 2012). This indicates that the outer density profile of the ejecta changes during the successive collisions with CSMs.

3. Mass-loss History

Hereafter, we consider the CSI-LW and CSI-LW plus ^{56}Ni models as our fiducial models. Given the fitting parameters

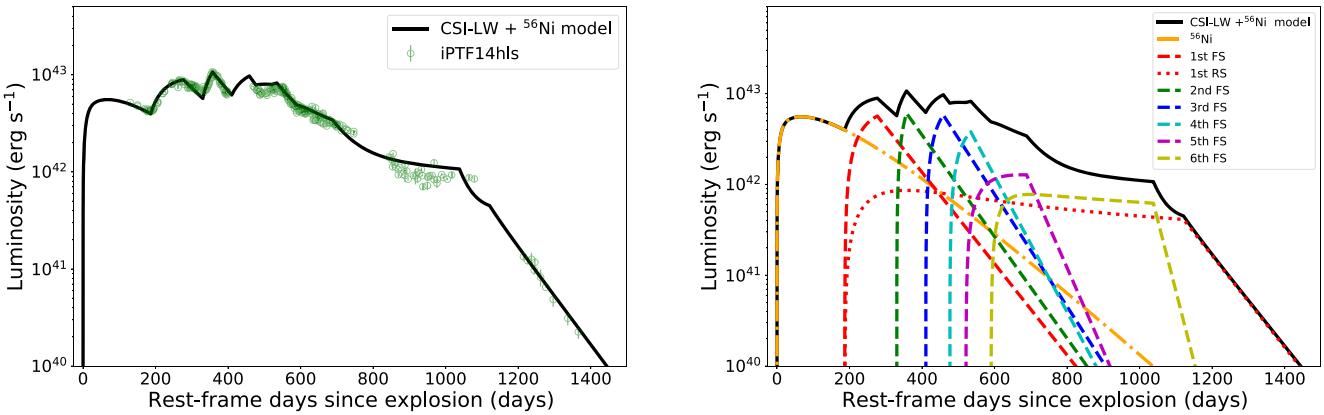


Figure 3. The fit to the bolometric luminosity (left panel) of iPTF14hls by the CSI-LW plus ^{56}Ni model. The contributions from the FSs, RS, and ^{56}Ni are plotted in the right panel. The FS emissions are plotted with the dashed lines, the first RS is plotted with the red dotted line, and the ^{56}Ni contribution is plotted with the orange dashed–dotted line.

Table 2
Model Parameters with the CSI Plus ^{56}Ni Model

Ejecta Properties						
$M_{\rm ej}(M_\odot)$	86					
$M_{\rm Ni}(M_\odot)$	0.9					
$v_{\rm SN}$ (km s^{-1})	5200					
δ	0					
n	7					
CSM Properties	1st	2nd	3rd	4th	5th	6th
$M_{\rm CSM}(M_\odot)$	18	15	25	20	35	80
$R_{\rm in}(10^{15}$ cm)	8.4	14.8	18	21	23	26
$\rho_{\rm in}(10^{-15}$ g cm^{-3})	8.5	7.3	5.4	5.2	4.1	1.1
$\epsilon_{\rm FS}$	0.07	0.14	0.1	0.08	0.04	0.018
$\epsilon_{\rm RS}$	0.26	0	0	0	0	0

listed in Tables 1 and 2, the mass-loss history of iPTF14hls can be studied. Before the discovery of iPTF14hls on 2014 September 22, there was a historic eruption at the same position of iPTF14hls on 1954 February 23 (Arcavi et al. 2017). Assuming that this eruption corresponds to the first CSM listed in Table 2, the wind velocity $v_{\rm wind}$ can be derived, namely $v_{\rm wind} = R_{\rm out,1}(1+z)/60.58$ yr $\simeq 42$ km s^{-1}, which is slightly higher than the observed wind velocity of Type II-P SNe (Smith 2014). Here, $R_{\rm out}$ is the outer radius of the CSM that is calculated according to $R_{\rm in}$, $M_{\rm CSM}$, and $\rho_{\rm in}$. If the initial decline of the light curve is attributed to ^{56}Ni decay, the wind velocity is $v_{\rm wind} \simeq 71$ km s^{-1}. Based on these wind velocities, we list the mass-loss history in Table 3.

All the timescales in Table 3 are calculated in the rest frame of the host galaxy of iPTF14hls, with the time zero-point set to the discovery date of iPTF14hls.[8] The mass-loss rates are $\dot{M} \simeq 0.4 - 1.3 M_\odot$ yr^{-1} (in the CSI-LW model) or $\dot{M} \simeq 0.85 - 3.3 M_\odot$ yr^{-1} (in the CSI-LW plus ^{56}Ni model), slightly higher than those of Type IIn (Schlegel 1990; Filippenko 1997) and Type IIn-P SNe (e.g., Kiewe et al. 2012; Taddia et al. 2013; Smith 2014).

In Table 3, we also list the outburst energies for each mass-loss episode, calculated according to $E_{\rm burst} = \frac{1}{2} M_{\rm CSM} v_{\rm wind}^2$. The burst energies have a typical value of $10^{47} - 10^{48}$ erg. These derived burst energies are small compared to the gravitational binding energies (see Equation (14) below) of the CSM shells before ejection. This indicates that there could be many more energy release episodes during the final evolution of the progenitor, where only a fraction of such energy release episodes trigger large-scale mass loss.

Waiting times are calculated as $T_{{\rm waiting},i} = T_{{\rm end},i} - T_{{\rm start},i-1}$ for the ith CSM. The durations and waiting times of the mass-loss episodes are presented in Figure 4. From Figure 4, we see that during the final 200 yr of evolution of the progenitor of iPTF14hls, mass loss is very frequent, with only very short quiescence periods (waiting times) following the longer wind-blowing episodes. An interesting exception is the last mass-loss episode (corresponding to the first CSM) in the CSI-LW plus ^{56}Ni model, where the waiting time $T_{\rm waiting} = 37.4$ yr is longer than the duration $T_{\rm duration} = 21.2$ yr. This waiting time is also much longer than the waiting times of earlier mass-loss episodes, which have values $T_{\rm waiting} = 1.9 - 7.6$ yr (see Figure 4 and Table 3). If the CSI-LW plus ^{56}Ni model is correct, this indicates that there could be a long quiescence before the final collapse of the progenitor.

It should be mentioned that the wind velocity is expected to increase as the progenitor becomes more and more compact, via shedding a large fraction of its mass. Taking this fact into account, the mass-loss rates of the earlier mass-loss episodes (the second to sixth CSMs listed in Table 3) could be lower and the durations and waiting times could be longer than the values given in Table 3. It is also possible that one or more of the CSM shells is the merging result of the late fast-moving shell running into the earlier slow-moving shell.

4. Discussion and Conclusions

The derived main-sequence mass ($M_{\rm zams} \simeq 245.5 M_\odot$) is consistent with a pair-instability SN (PISN; Barkat et al. 1967; Rakavy & Shaviv 1967; Ober et al. 1983; Bond et al. 1984; Glatzel et al. 1985; Scannapieco et al. 2005; Kasen et al. 2011), which has a mass range $140 M_\odot < M_{\rm zams} < 260 M_\odot$. However, theoretical studies suggest that massive stars with $M_{\rm zams} \simeq 245.5 M_\odot$ will end their lives during the final explosions in which they disrupt themselves completely, meaning that they do not episodically lose mass. In this case, the CSM shells listed in Table 2 may be generated by envelope instabilities (Yoon & Cantiello 2010; Owocki 2015), which have been

[8] A more appropriate zero-point time may be the explosion time of iPTF14hls. However, given the large uncertainty of the explosion time, here we just use the discovery date. This approximation only introduces a very minor error in the derived quantities.

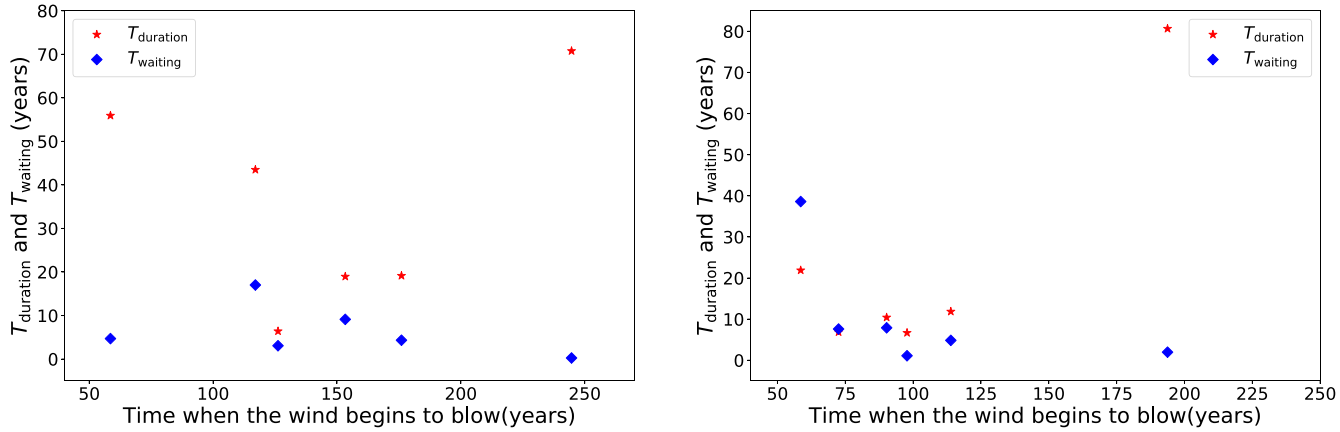


Figure 4. The durations and waiting times of the mass-loss episodes in the CSI-LW (left panel) and CSI-LW plus ^{56}Ni (right panel) models.

Table 3
The Mass-loss History of iPTF14hls Derived According to the CSI-LW and CSI-LW Plus ^{56}Ni Models

		CSI-LW model						CSI-LW Plus ^{56}Ni Model					
		1st	2nd	3rd	4th	5th	6th	1st	2nd	3rd	4th	5th	6th
$\dot{M}$	($M_\odot$ yr^{-1})	0.37	0.6	1.3	1.3	1.2	1.0	0.85	2.3	2.5	3.3	3.1	1.0
T_{start}	(yr)	58.6	117.1	126.2	152.3	176.0	244.7	58.6	72.5	90.2	99.7	113.9	193.8
T_{end}	(yr)	4.5	75.0	120.0	133.5	157.5	176.3	37.4	65.9	80.2	93.5	102.4	115.8
$T_{duration}$	(yr)	54.1	42.1	6.2	18.7	18.5	68.4	21.2	6.6	10.1	6.2	11.5	78.0
$T_{waiting}$	(yr)	4.5	16.5	3.0	7.3	5.3	0.2	37.4	7.4	7.6	3.3	2.8	1.9
E_{burst}	(10^{47} erg)	3.6	4.5	1.4	4.4	3.9	12.4	9.1	7.5	12.6	10.1	17.6	40.3

Note. $\dot{M}$ is the mass-loss rate and T_{start}, T_{end}, $T_{duration}$, $T_{waiting}$, and E_{burst} are the start time, end time, duration, waiting time, and burst energy of the mass-loss episodes, respectively. All times are in the rest frame of the host galaxy.

suggested for the mass loss of some Type II-P SNe in their final stage of evolution (e.g., Rui et al. 2019). Another difficulty for the interpretation of iPTF14hls as a PISN is that the derived ^{56}Ni mass $M_{Ni} = 0.9M_\odot$ (see Table 2) in the CSI-LW plus ^{56}Ni model is lower than the expected yield of ^{56}Ni during the final disruptive explosion of a PISN, which could have $M_{Ni} \sim 50M_\odot$ for a $M_{zams} \simeq 250M_\odot$ star (Heger & Woosley 2002; Umeda & Nomoto 2002).

The properties of the progenitor of iPTF14hls are more consistent with a pulsational PISN[9] (PPISN; Barkat et al. 1967; Woosley et al. 2007; Chen et al. 2014; Woosley & Heger 2015), as discussed in the literature (Arcavi et al. 2017; Woosley 2018). There may be some overlap between the initial mass of a star that will end up as a PISN or a PPISN, which has a mass range $70M_\odot < M_{zams} < 140M_\odot$. This is plausible because our current understanding of massive star evolution is incomplete, owing to the complex physics involved, including metallicity-related mass loss, chemical mixing, rotation, binary interaction–related mass transfer, and magnetic torques (Ohkubo et al. 2009; Chatzopoulos & Wheeler 2012; Woosley 2017; Leung et al. 2019; Marchant et al. 2019; Woosley 2019). Indeed, Yoshida et al. (2016) calculated the evolutions of stars with metallicity $Z = 0.004$ and initial masses of 140, 200, and $250M_\odot$, which are well within the usually assumed mass range of PISNe. They found that their masses decrease to 54, 59, and $61M_\odot$ before the neon burning owing to mass loss. Eventually, the above three stars experience six ($M = 140M_\odot$) to three ($M = 250M_\odot$) episodes of mass loss induced by pulsational pair-instability during their final 1 ($M = 140M_\odot$) to 1400 ($M = 250M_\odot$) yr evolution before core collapse.

For a star that will end up as a PPISN, electron–positron pairs will be generated when the central temperature of the massive helium core rises to $(1.8 - 2.3) \times 10^9$ K (Fowler & Hoyle 1964; Barkat et al. 1967; Rakavy & Shaviv 1967). The sudden loss of pressure due to the production of electron–positron pairs leads to the contraction of the helium core. Then explosive burning of oxygen ensues, so as to eventually reverse the contraction of the core to expansion. Such pulsational activity becomes more and more energetic, to shed some amount of envelope, during the final evolution of a PPISN progenitor. The duration of the pulsational activity spans a wide range of time, from a few hours to 10^4 yr (Woosley 2017), in accordance with the mass-loss history listed in Table 3.

During the pair pulsation, the progenitor of a PPISN may be an RSG, a blue supergiant (BSG), a luminous blue variable, or a Wolf–Rayet star, if the hydrogen envelope is completely shed away by continuous mass loss (Woosley 2017). The gravitational binding energy of the hydrogen shell that will be blown away by the pulsation is

$$E_p = 1.2 \times 10^{49}\ \mathrm{erg}\left(\frac{M_R}{150M_\odot}\right)\left(\frac{M_s}{30M_\odot}\right) \times \left(\frac{R_p}{10^{14}\ \mathrm{cm}}\right)^{-1}, \quad (14)$$

[9] Because of mass loss, the metallicity of the progenitor of iPTF14hls should be $Z \leqslant 0.5Z_\odot$ (Langer et al. 2007; Georgy et al. 2013; Yusof et al. 2013; Spera et al. 2015; Leung et al. 2019) to form an He core massive enough to undergo pulsational pair-instability. This results in an opacity κ essentially identical to our adopted value, because electron-scattering opacity depends on metallicity very weakly.

where M_s is the shell mass that will be blown away, M_R is the mass left over after mass shedding, and R_p is the radius of the progenitor star during helium burning. $R_p \approx 10^{14}$ cm if the progenitor star is an RSG, while $R_p \approx 10^{13}$ cm for a BSG. The progenitor of iPTF14hls is likely an RSG, since the above binding energy is closer to the burst energies listed in Table 3. For the same reason, the initial decline of the light curve could be more likely attributed to ^{56}Ni decay, since in the CSI-LW plus ^{56}Ni model the burst energies are closer to the binding energy.

The amount of ^{16}O burnt during one pulsation can be estimated as

$$M_{\rm O} = 0.01 M_{\odot} \left(\frac{E_p}{10^{49}\ {\rm erg}} \right). \quad (15)$$

Here, the energy release by ^{16}O burning is 0.52 MeV per nucleon (Arnett 1996; Wallerstein et al. 1997). The contraction timescale of the helium core is the dynamical timescale. Therefore, such an amount of ^{16}O will be burnt in

$$t_d = 3.8\ {\rm hr} \left(\frac{R_c}{10^{12}\ {\rm cm}} \right)^{3/2} \left(\frac{M_c}{50 M_{\odot}} \right)^{-1/2}, \quad (16)$$

where R_c and M_c are the radius and mass of the helium core that participates in the pulsation. The timescales of the mass ejection and subsequent resettlement to a new bound state are the Kelvin–Helmholtz timescale, i.e., several years (see Table 3), which is much longer than the dynamical timescale given by Equation (16).

It is usually assumed that the remnants of PPISNe are massive black holes and that no ^{56}Ni is ejected to power the SN light curve (e.g., Woosley 2017; Leung et al. 2019). Tolstov et al. (2017), on the other hand, propose that a PPISN can eject a large amount of ^{56}Ni ($M_{\rm Ni} = 6 M_{\odot}$) to power the light curve of SLSN PTF12dam, despite the formation of a black hole in PTF12dam. Given the moderate amount of ^{56}Ni in the CSI-LW plus ^{56}Ni model (see Table 2), we suggest that the ^{56}Ni may be ejected during the collapse of the helium core to a massive black hole, i.e., a collapsar (Woosley 1993). This implies the rapid rotation of the helium core. However, such a rapid rotation is in tension with the existence of the hydrogen-rich envelope of the progenitor of iPTF14hls, since rotation tends to remove the hydrogen envelope. This tension can be relaxed by assuming a differential rotation of the progenitor star. The derived explosion energy (Equation (13)) is also consistent with the collapsar model.

To date, there are several candidates for PPISNe (Ben-Ami et al. 2014; Lunnan et al. 2018; Gomez et al. 2019). Nicholl et al. (2020) reported the detection of a Type IIn SLSN 2016aps with energy $E_{\rm SN} \gtrsim 10^{52}$ erg and a total mass (ejecta+CSM) exceeding $50 - 100 M_{\odot}$. Detailed one-dimensional radiation-hydrodynamic simulations (Suzuki et al. 2021) suggest that SN 2016aps could be a collision of an ejecta mass $M_{\rm ej} = 30 M_{\odot}$ with an $M_{\rm CSM} \simeq 8 M_{\odot}$ wind-like CSM of outer radius 10^{16} cm. SN 2016aps has a radiated energy $E_{\rm rad} \gtrsim 5 \times 10^{51}$ erg, which is an order of magnitude higher than iPTF14hls. The mass-loss rate of SN 2016aps, $\dot{M} \approx 0.3 M_{\odot}\ {\rm yr}^{-1}$, assuming a wind velocity $u_w = 100\ {\rm km\ s}^{-1}$, is comparable to that of iPTF14hls. Yang et al. (2021) reported the Type II SN 2020faa, whose first six months of light curves are of great similarity to those of iPTF14hls.

The light curve of iPTF14hls is very unusual among the SNe studied so far. In this paper, we explore the possibility of interpreting iPTF14hls as a multiple-interaction-powered SN. We find that within reasonable parameters, the theoretical light curve matches well with the light curve of iPTF4hls. This makes iPTF14hls a possible candidate for a PPISN. Moriya et al. (2020) proposed that iPTF14hls is produced by a continuous outflow like a stellar wind, rather than a mass ejection. They calculated the mass-loss rates of iPTF14hls as high as $10 M_{\odot}\ {\rm yr}^{-1}$ in the bright phase. Such an extreme mass-loss rate is much higher than the results obtained from our calculations. Dessart (2018) found that magnetar-powered SN ejecta reproduce some of the observed properties of iPTF14hls, including the sustained brightness in the R band, the blue optical color, and the broad HI lines. With the magnetar model, however, it is difficult to produce fluctuating light curves with multiple peaks, unless the variable thermal energy injection from magnetar spin-down is considered (Moriya et al. 2022). In the future, more observations and improved theoretical modeling can improve our understanding of very massive stars (Heger et al. 2003).

We thank the anonymous referee for the constructive comments that allowed us to improve the paper significantly. We also thank Iair Arcavi and Jesper Sollerman for providing us with the observational data. This work is supported by the National Program on Key Research and Development Project of China (Grant Nos. 2021YFA0718500 and 2017YFA0402600), and the National Natural Science Foundation of China (Grant Nos. U1938201, 11833003, and 12103055). X.F.W. is supported by the National Natural Science Foundation of China (NSFC grants 12033003 and 11633002), the Major State Basic Research Development Program (grant 2016YFA0400803), and the Scholar Program of the Beijing Academy of Science and Technology (DZ:BS202002).

ORCID iDs

Ling-Jun Wang https://orcid.org/0000-0002-8352-1359
Liang-Duan Liu https://orcid.org/0000-0002-8708-0597
Xiao-Feng Wang https://orcid.org/0000-0002-7334-2357
Zi-Gao Dai https://orcid.org/0000-0002-7835-8585
Bing Li https://orcid.org/0000-0002-0238-834X
Li-Ming Song https://orcid.org/0000-0003-0274-3396

References

Andrews, J. E., & Smith, N. 2018, MNRAS, 477, 74
Arnett, W. D. 1982, ApJ, 253, 785
Arnett, D. 1996, Supernovae and Nucleosynthesis: An Investigation of the History of Matter from the Big Bang to the Present (Princeton, NJ: Princeton Univ. Press), 112
Arcavi, I., Howell1, D. A., Kasen, D., et al. 2017, Natur, 551, 210
Barkat, Z., Rakavy, G., & Sack, N. 1967, PhRvL, 18, 379
Ben-Ami, S., Gal-Yam, A., Mazzali, P. A., et al. 2014, ApJ, 785, 37
Bond, J. R., Arnett, W. D., & Carr, B. J. 1984, ApJ, 280, 825
Bruch, R. J., Gal-Yam, A., Schulze, S., et al. 2021, ApJ, 912, 46
Chatzopoulos, E., & Wheeler, J. C. 2012, ApJ, 748, 42
Chatzopoulos, E., Wheeler, J. C., & Vinko, J. 2012, ApJ, 746, 121
Chen, K.-J., Woosley, S., Heger, A., Almgren, A., & Whalen, D. J. 2014, ApJ, 792, 28
Chevalier, R. A. 1982, ApJ, 258, 790
Chevalier, R. A., & Fransson, C. 1994, ApJ, 420, 268
Chugai, N. N. 2018, AstL, 44, 370
Chugai, N. N., & Danziger, I. J. 1994, MNRAS, 268, 173
Colgate, S. A., Petschek, A. G., & Kriese, J. T. 1980, ApJL, 237, L81
Dessart, L. 2018, A&A, 610, L10
Filippenko, A. V. 1997, ARA&A, 35, 309

Fowler, W. A., & Hoyle, F. 1964, ApJS, 9, 201
Gal-Yam, A. 2012, Sci, 337, 927
Gal-Yam, A. 2019, ARA&A, 57, 305
Gal-Yam, A., Arcavi, I., Ofek, E. O., et al. 2014, Natur, 509, 471
Gal-Yam, A., Bruch, R., Schulze, S., et al. 2022, Natur, 601, 201
Georgy, C., Ekstrtröm, S., Eggenberger, P., et al. 2013, A&A, 558, A103
Glatzel, W., Fricke, K. J., & El Eid, M. F. 1985, A&A, 149, 413
Gofman, R. A., & Soker, N. 2019, MNRAS, 488, 5854
Gomez, S., Berger, E., Nicholl, M., et al. 2019, ApJ, 881, 87
Heger, A., Fryer, C. L., Woosley, S. E., et al. 2003, ApJ, 591, 288
Heger, A., & Woosley, S. E. 2002, ApJ, 567, 532
Hosseinzadeh, G., Berger, E., Metzger, B. D., et al. 2021, arXiv:2109.09743
Hosseinzadeh, G., Valenti, S., McCully, C., et al. 2018, ApJ, 861, 63
Inserra, C. 2019, NatAs, 3, 697
Jacobson-Galá, N. W. V., Dessart, L., Jones, D. O., et al. 2022, ApJ, 924, 15
Kaplan, N., & Soker, N. 2020, MNRAS, 492, 3013
Kasen, D., Woosley, S. E., & Heger, A. 2011, ApJ, 734, 102
Khazov, D., Yaron, O., Gal-Yam, A., et al. 2016, ApJ, 818, 3
Kiewe, M., Gal-Yam, A., Arcavi, I., et al. 2012, ApJ, 744, 10
Langer, N., Norman, C. A., de Koter, A., et al. 2007, A&A, 475, L19
Leung, S.-C., Blinnikov, S., Nomoto, K., et al. 2020, ApJ, 903, 66
Leung, S.-C., Fuller, J., & Nomoto, K. 2021, ApJ, 915, 80
Leung, S.-C., Nomoto, K., & Blinnikov, S. 2019, ApJ, 887, 72
Li, L., Wang, S. Q., Liu, L. D., et al. 2020, ApJ, 891, 98
Li, W. X., Wang, X. F., & Zhang, T. M. 2015, ATel, 6898, 1
Liu, L.-D., Wang, L.-J., & Gao, H. 2020, RNAAS, 4, 162
Liu, L. D., Wang, L. J., Wang, S. Q., & Dai, Z. G. 2018, ApJ, 856, 59
Liu, T., Song, C.-Y., Yi, T., Gu, W.-M., & Wang, X.-F. 2019, JHEAp, 22, 5
Lunnan, R., Fransson, C., Vreeswijk, P. M., et al. 2018, NatAs, 2, 887
Marchant, P., Renzo, M., Farmer, R., et al. 2019, ApJ, 882, 36
Matzner, C. D., & McKee, C. F. 1999, ApJ, 510, 379
Modjaz, M., Gutiérrez, C. P., & Arcavi, I. 2019, NatAs, 3, 717
Moriya, T. J., Blinnikov, S. I., Tominaga, N., et al. 2013a, MNRAS, 428, 1020
Moriya, T. J., Maeda, K., Taddia, F., et al. 2013b, MNRAS, 435, 1520
Moriya, T. J., Murase, K., Kashiyama, K., et al. 2022, MNRAS, 513, 6210
Moriya, T. J., Mazzali, P. A., & Pian, E. 2020, MNRAS, 491, 1384
Moriya, T. J., Sorokina, E. I., & Chevalier, R. A. 2018, SSRv, 214, 59
Nicholl, M., Blanchard, P. K., Berger, E., et al. 2020, NatAs, 4, 893
Ober, W. W., El Eid, M. F., & Fricke, K. J. 1983, A&A, 119, 61
Ohkubo, T., Nomoto, K., Umeda, H., Yoshida, N., & Tsuruta, S. 2009, ApJ, 706, 1184
Owocki, S. P. 2015, in Very Massive Stars in the Local Universe, ed. J. S. Vink, Vol. 412 (Berlin: Springer), 113
Parker, E. N. 1961, ApJ, 133, 1014
Pellegrino, C., Howell, D. A., Vinkó, J., et al. 2022, ApJ, 926, 125
Quimby, R. M., Kulkarni, S. R., Kasliwal, M. M., et al. 2011, Natur, 474, 487
Quimby, R. M., Wheeler, J. C., Höflich, P., et al. 2007, ApJ, 666, 1093
Rakavy, G., & Shaviv, G. 1967, ApJ, 148, 803
Rui, L. M., Wang, X. F., Mo, J., et al. 2019, MNRAS, 485, 1990
Scannapieco, E., Madau, P., Woosley, S., Heger, A., & Ferrara, A. 2005, ApJ, 633, 1031
Schlegel, E. M. 1990, MNRAS, 244, 269
Smith, N. 2014, ARA&A, 52, 487
Smith, N. 2017, in Handbook of Supernovae, ed. A. W. Alsabti & P. Murdin (Berlin: Springer), 403
Soker, N., & Gilkis, A. 2018, MNRAS, 475, 1198
Sollerman, J., Taddia, F., Arcavi, I., et al. 2019, A&A, 621, A30
Spera, M., Mapelli, M., & Bressan, A. 2015, MNRAS, 451, 4086
Suzuki, A., Moriya, T. J., & Takiwaki, T. 2019, ApJ, 887, 249
Suzuki, A., Nicholl, M., Moriya, T. J., & Takiwaki, T. 2021, ApJ, 908, 99
Swartz, D. A., Sutherland, P. G., & Harkness, R. P. 1995, ApJ, 446, 766
Taddia, F., Stritzinger, M. D., Sollerman, J., et al. 2013, A&A, 555, A10
Tolstov, A., Nomoto, K., Blinnikov, S., et al. 2017, ApJ, 835, 266
Tolstov, A., Nomoto, K., Sorokina, E., et al. 2019, ApJ, 881, 35
Umeda, H., & Nomoto, K. 2002, ApJ, 565, 385
Uno, K., & Maeda, K. 2020, ApJ, 897, 156
van Marle, A. J., Smith, N., Owocki, S. P., & van Veelen, B. 2010, MNRAS, 407, 2305
Wallerstein, G., Iben, I., Jr., Parker, P., et al. 1997, RvMP, 69, 995
Wang, L. J., Wang, X. F., Wang, S. Q., et al. 2018, ApJ, 865, 95
Wang, L. J., Wang, X. F., Cano, Z., et al. 2019a, MNRAS, 489, 1110
Wang, S. Q., Gan, W.-P., Li, L., et al. 2019b, arXiv:1904.09604
Wang, L. J., & Yu, H. 2022, CatFit: Calculate the Bolometric Luminosity of an SN with Multiple Ejecta-CSM Interactions, v1.0.0, Zenodo, doi:10.5281/zenodo.6508082
Wang, S. Q., Liu, L. D., Dai, Z. G., Wang, L. J., & Wu, X. F. 2016, ApJ, 828, 87
Wheeler, J. C., Chatzopoulos, E., Vinkó, J., et al. 2017, ApJL, 851, L14
Woosley, S. E. 1993, ApJ, 405, 273
Woosley, S. E. 2017, ApJ, 836, 244
Woosley, S. E. 2018, ApJ, 863, 105
Woosley, S. E. 2019, ApJ, 878, 49
Woosley, S. E., Blinnikov, S., & Heger, A. 2007, Natur, 450, 390
Woosley, S. E., & Heger, A. 2015, in Very Massive Stars in the Local Universe, ed. J. S. Vink, Vol. 412 (Berlin: Springer), 199
Xiang, D. F., Wang, X. F., Lin, W. L., et al. 2021, ApJ, 910, 42
Yang, S., Sollerman, J., Chen, T.-W., et al. 2021, A&A, 646, A22
Yaron, O., Perley, D. A., Gal-Yam, A., et al. 2017, NatPh, 13, 510
Yoon, S.-C., & Cantiello, M. 2010, ApJL, 717, L62
Yoshida, T., Umeda, H., Maeda, K., & Ishii, T. 2016, MNRAS, 457, 351
Yuan, Q., Liao, N. H., Xin, Y. L., et al. 2018, ApJL, 854, L18
Yusof, N., Hirschi, R., Meynet, G., et al. 2013, MNRAS, 433, 1114